Structural Correlations and Motifs in Liquid Water at Selected Temperatures: Ab Initio and Empirical Model Predictions[†]

Yves A. Mantz,*,‡,§ Bin Chen,∥ and Glenn J. Martyna*,§

IBM T. J. Watson Research Lab−Yorktown, Route 134 and P.O. Box 218,
Yorktown Heights, New York 10598-0218, and Department of Chemistry,
Louisiana State University, Baton Rouge, Louisiana 70803-1804

To gain further insight into liquid water's structure and explore the role of different physical forces underlying the interaction between water molecules, the radial and angular structure of water is probed as a function of temperature for a carefully selected set of theoretical models. Simulations are performed with empirical rigid, empirical polarizable, empirical flexible with classical and quantum nuclei, and ab initio models with classical nuclei at 300 and 353 K and quantum nuclei at 300 K. The predicted radial distribution functions, spatial maps, and angular distributions of the neighboring water molecules are consistent with a model of liquid water in which water molecules are tetrahedrally coordinated. In addition, three-dimensional joint distribution functions are introduced and analyzed. By comparison of the functions obtained for hexagonal ice to those of liquid water, several thermally disordered, icelike cluster structures are identified in the fluid.

I. Introduction

Developing a detailed understanding of the structure of neat liquid water is an important goal of physical chemistry. Structural features in this complex fluid have been proposed to explain water's unusual temperature-dependent properties,[1] which have far-reaching consequences for life. A knowledge of water's structure is also needed to test the assumptions made in constructing different models of the hydrogen bond, a primary driving force that governs water's ability to act as a polar solvent and influences the structural, dynamical, and chemical properties of hydrophilic and hydrophobic solutes.

A qualitative understanding of liquid water's radial and angular structure has been established through several landmark experimental[2] and theoretical[3] studies. The ordered lattice of hexagonal ice I_h is broken up into a fluctuating network of hydrogen-bonded molecules in the neat liquid. The nearest-neighbor solvation shell, consisting of four molecules on average at ∼300 K in a tetrahedral arrangement, is interspersed with interstitial water molecules between the first and the second shell. Structural correlations beyond the third shell are very weak. At present, a consensus on the quantitative radial[4,5] and angular[6] distribution of the molecules in liquid water is beginning to emerge, amidst some dissenting views and controversy.[7−11] One approach to resolve uncertainty and clarify unresolved issues would be to simulate a sufficiently large model system with a highly accurate theoretical method, which is, unfortunately, impractical. However, considerable insight into water's structure can still be gained by simulating a well-chosen set of theoretical models with different physics included and carefully considering the results. This goal is partially addressed in our recent letter,[12] in which a subset of structural predictions are compared to the latest experimental results.[4−7]

Accordingly, the objective of this work is an enhanced understanding of water structure and the physical "forces"−including the charge distribution, polarizability, nuclear quantum effects, and molecular flexibility−affecting this structure. A high-level treatment of liquid water is achieved by performing ab initio molecular dynamics (AIMD), in which the valence electronic structure is calculated "on the fly"[13,14] from an extended Lagrangian whose energy terms are taken from density functional theory (DFT), at the BLYP level. In principle, DFT is able to provide the exact ground-state energy, identical to that obtained from the Schrödinger equation. Unfortunately, the correct form of the exchange−correlation energy functional is not yet known, so an approximate form must still be chosen. The approximate BLYP functional (section II) provides a good description of the molecular charge distribution and the molecular polarizability beyond the dipole approximation. However, it is also well-known that BLYP does not describe dispersion well, and it is an open question as to how well it can describe complex environments such as liquid water.

In addition, several of the most popular empirical water models are selectively chosen from the literature and compared to separate out the major "forces" determining structure. The influence of the charge arrangement is examined by comparing three widely used, *empirical rigid* models, TIP3P,[15] TIP4P,[15] and TIP5P,[16] differing in their description of the molecular charge distribution. The hydrogen atoms are positively charged, $+\delta = 0.417e$ (TIP3P), $0.520e$ (TIP4P), and $0.241e$ (TIP5P), but the negative charge of -2δ is either assigned to oxygen (TIP3P), moved slightly along the bisector of the HOH angle toward the hydrogen atoms (TIP4P), or split in half and placed at the corners of a tetrahedron to mimic the lone pairs (TIP5P). (Although new parametrizations of these models for use with Ewald summation are now available,[17−19] the original models are retained here because of their prevalence in the literature and the expectation that *differences* in structural changes resulting from physics added to TIP4P versus TIP4P-Ew will not be significant.) The influence of intramolecular stretching and bending modes is evaluated by comparison to an *empirical flexible* model, TIP4P-flex,[20] with an anharmonic TIP4P mono-

Structural Correlations and Motifs in Water

J. Phys. Chem. B, Vol. 110, No. 8, 2006 **3541**

TABLE 1: Major Simulation Studies of Pure Liquid Water, Excluding Those at 323 K for Brevity[a]

force field	N_{H_2O}	L_{300} (Å)	L_{353} (Å)	$\mathcal{T}$(ps)	δt (fs)
BLYP	32	9.865	9.948	60	0.125
BLYP[b]	64	12.419		10	0.121
BLYP-PI[c]	64	12.419		15	0.121
TIP3P	256	19.730	19.896	15000	6.0
TIP4P	128	15.660	15.792	1200	6.0
TIP4P-flex	128	15.660	15.792	1200	1.0
TIP4P-flex-PI	128	15.660	15.792	200	1.0
TIP4P-pol-2	500	24.630[d]	24.972[d]		
TIP5P	500	24.783[d]	25.206[d]		

[a] Symbols are defined and force fields are referenced in the text. [b] Reference 29. [c] Reference 30. [d] Average value during a MC simulation in the NPT ensemble.

mer. Nuclear quantum effects are probed via path-integral simulations of the TIP4P-flex model, denoted TIP4P-flex-PI, where each "quantum" nucleus is isomorphic to a classical ring polymer of $P = 64$ beads (Appendix A). Last, the role of polarizability, or a molecule's electronic response to the changing electric field of the other molecules, at nonambient temperature is studied using an *empirical polarizable* (or fluctuating-charge) model, TIP4P-pol-2.[21]

The organization of this paper is as follows: The simulation details are given in section II. The radial (section III), spatial (section IV), and angular (section V) structures predicted by the different theoretical models are then compared. Joint probability distributions are introduced in section VI and used to identify the most prevalent configurations in liquid water. Their use in this context is further intended to illustrate their potential application for identifying the most likely molecular configurations in other disordered media. Conclusions are drawn in section VII.

II. Computational Models and Methods

In this section, the simulations performed with the above models are described. Important simulation details, including the number of water molecules, N_{H_2O}, in the periodic cubic box of length L at temperature T, L_T, the data collection period, $\mathcal{T}$, and the simulation time step, δt, are summarized in Table 1. Section II is concluded by a discussion of the analysis of statistical uncertainty in configuration sampling and finite-size effects.

Like all theoretical methods in practice, the AIMD simulations performed in this work are not exact. Here, the "AIMD (BLYP/pw)" results are obtained within the generalized gradient approximation (GGA) of density functional theory, at the BLYP[22] level (whose empirical constants are system-independent), with atomic pseudopotentials[23] and a plane-wave (pw) basis set truncated at $E_{cut} = 70$ Ry and a single k-point (Γ-point), as implemented in PINY_MD.[24] To improve adiabaticity, the hydrogen masses are set equal to 15.9994 a.u., preserving all static properties for classical nuclei. Also, a preconditioning scheme is employed,[25] such that the electronic fictitious "mass", μ, is raised above 400 a.u. for high-energy/frequency components of the plane-wave expansion that might couple to the nuclei efficiently. The convergence of all results with respect to μ is verified elsewhere.[12] For better temperature control, the ions are "massively" thermostated, employing one Nosé−Hoover thermostat[26,27] per ionic degree of freedom, while the electronic equations of motion are integrated using the NORB scheme,[28] permitting independent-state thermostating of every (doubly occupied) Kohn−Sham orbital. An equilibration period of at least 14 ps at 300 K or 5 ps at either 323 or 353 K is required starting from a TIP3P configuration, based on structural

analyses. Last, all structural predictions from a third simulation performed at 323 K, $L_{323} = 9.894$ Å, are intermediate in value between those at 300 and 353 K. This simulation protocol is designed and optimized specifically to study the thermodynamic (structural) properties of water, but the tradeoff is that the dynamical information from the simulations is corrupted (i.e., correlation functions of a time sequence) upon choosing "heavy" atoms and thermostats. Results are also taken from a run with 64 H_2O molecules[29] and a path-integral simulation, AIPI (BLYP/pw), with $P = 16$ beads and an 80 Ry cutoff.[30]

The empirical model simulation details are also important. With the TIP3P, TIP4P, TIP4P-flex, and TIP4P-flex-PI force fields, the sampling method is molecular dynamics (MD) or path-integral molecular dynamics (PI) in the NVT ensemble; alternatively, Monte Carlo (MC) in the NPT ensemble is the method of choice using the TIP4P-pol-2 and TIP5P force fields. The MD simulations are performed using PINY_MD.[24] The MC simulations are carried out as described in ref 31. In particular, for simulations with the TIP4P-pol-2 force field, the adiabatic separation of the nuclear and electronic degrees of freedom is achieved by the adiabatic nuclear and electronic sampling MC (ANES-MC) algorithm. The conditions are such[31] that the nuclear and electronic degrees of freedom are sampled independently and accepted/rejected using the Metropolis rule with the same temperature, T, similar to the sequential-fluctuating-charge MC (SFQ-MC) algorithm.[32] The frequency of the volume move is adjusted to yield 1 accepted move per 10 MC cycles. The remainder of the moves are equally divided between translation of the center-of-mass, rotation around the center-of-mass, and the electronic move (i.e., the ratio of electronic to nuclear moves is $R_{elec} = 1$). Note that electronic moves are required only for the TIP4P-pol-2 force field but not for the nonpolarizable TIP5P model. The maximum displacement for each type of MC move is adjusted to yield an acceptance rate of roughly 50%. The production length for the MC simulations is 500 000 cycles, with $N_{H_2O} = 500$ moves per cycle.

The error in the simulation results is carefully considered. The distance-dependent error bars, $\sigma(r)$, given in Figures 1 and 2, or the angle-dependent error bars, $\sigma(\theta)$, in Figures 5 and 6, that are bracketing the TIP4P results are, in fact, providing an estimate of the error in the AIMD (BLYP/pw) results. They are calculated by, first, performing several ($N_{sim} = 20$) TIP4P simulations with the same system size, N_{H_2O}, time step, δt, and data collection period, $\mathcal{T}$, as in the AIMD (BLYP/pw) simulations. Subsequently, the ($N_{sim} = 20$) $g(r)$ or $P(\theta)$ values obtained from these TIP4P simulations are averaged, enabling the calculation of either $\sigma(r)$ or $\sigma(\theta)$. For example, the error in the AIMD (BLYP/pw) oxygen−oxygen radial distribution function, $g_{OO}(r)$, at 300 K is estimated by performing $N_{sim} = 20$ TIP4P simulations, each 60 ps in duration with 32 H_2O molecules, determining 20 TIP4P $g_{OO}(r)$ values, and then calculating $\sigma(r)$. Note that TIP4P is significantly better than the TIP3P model in predicting water structure and fairly representative of the AIMD (BLYP/pw) structural predictions. The corresponding error in the TIP4P $g(r)$ itself, calculated from the trajectory of length, $N_{sim}\mathcal{T}$, is $\sigma_m(r) = \sigma(r)/\sqrt{N_{sim}}$. A similar formula is used to estimate the error in TIP4P $P(\theta)$ and may also be applied to estimate the uncertainty in simulations of arbitrary length. In general, both σ and σ_m are quite small, and smoothing/filtering of the results in sections III−V is not performed after checking convergence with respect to bin width.[33] However, very long runs would be required to achieve full convergence of the calculated spatial maps (section IV) and three-dimensional (3D) distribution functions (section VI) because of their high
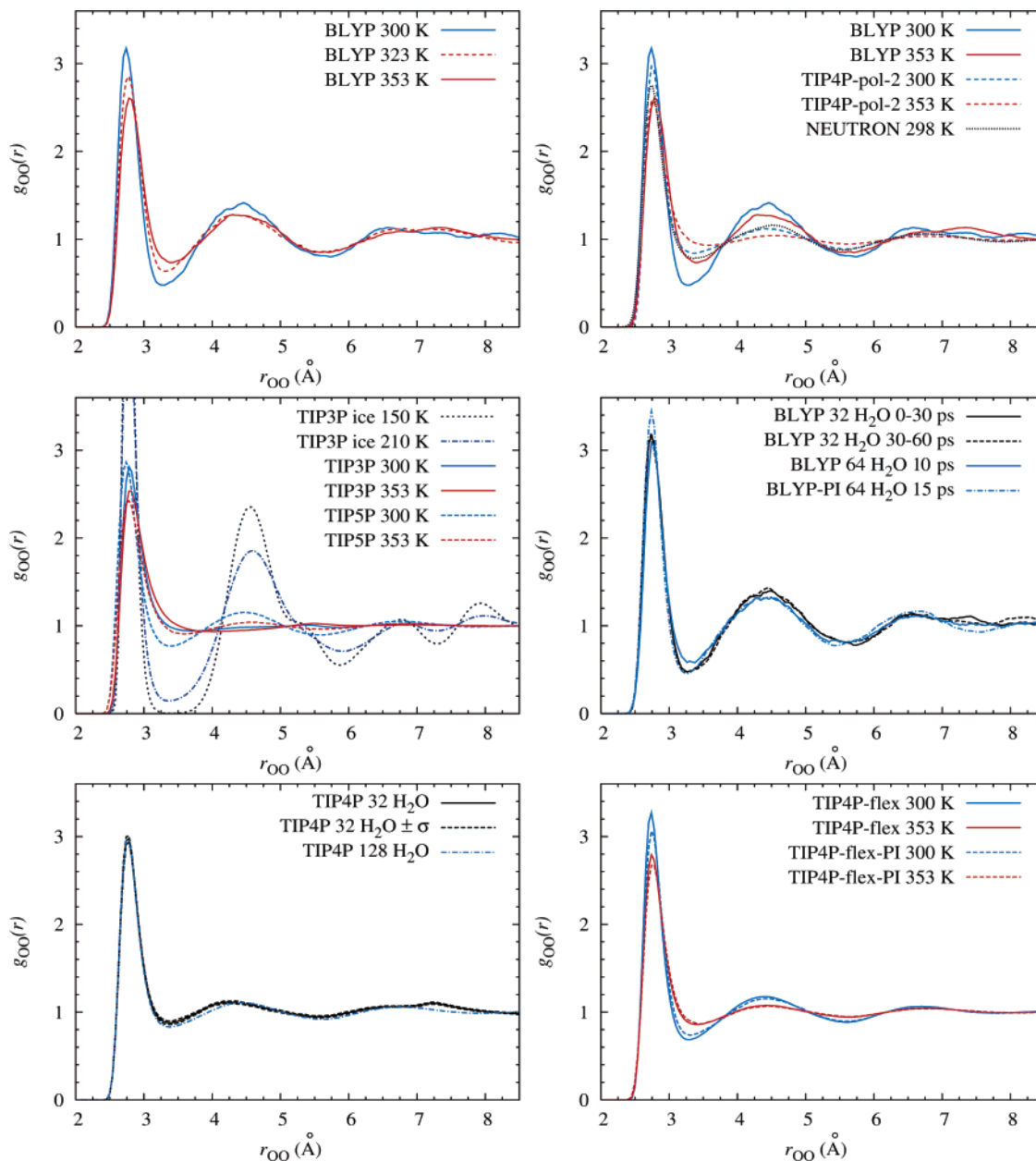
Figure 1. Water and ice I_h $g_{OO}(r)$ values (0.04 Å bin). Neutron data from ref 5.

TABLE 2: $g_{OO}(r)$ First Peak Height at r_{OO}^{max} and the Coordination Number, $n_{OO}(r)$, at r_{OO}^{min}, the First Local Minimum of $g_{OO}(r)$

	TIP3P		TIP4P		-flex		-flex-PI		-pol-2		TIP5P		AIMD		AIPI
T (K)	300	353	300	353	300	353	300	353	300	353	300	353	300	353	300
r_{OO}^{max} (Å)	2.78	2.78	2.78	2.78	2.74	2.74	2.74	2.78	2.74	2.78	2.74	2.78	2.74	2.78	2.74
$g(r_{OO}^{max})$	2.8	2.5	3.0	2.6	3.3	2.8	3.1	2.7	3.0	2.6	2.9	2.4	3.2	2.6	3.4
r_{OO}^{min} (Å)	3.34	3.34	3.22	3.30	3.22	3.26	3.22	3.26	3.22	3.30	3.26	3.34	3.22	3.30	3.22
$n(r_{OO}^{min})$	4.7	4.6	4.1	4.3	4.1	4.1	4.1	4.1	4.0	4.2	4.1	4.2	4.1	4.2	4.0

dimensionality. Accordingly, the 3D functions are smoothed by applying a moving window average (Savitzky−Golay (0,2,2) filter) first to the cosine terms at every distance (or r_{OH}) greater than 2.5 Å and then to these distances at each cosine value. This filtering procedure is applied once to the empirical model results and twice to the AIMD (BLYP/pw) model results in section VI. Last, throughout this work, finite-size effects are probed by comparing predictions from nanosecond-length simulations with 32, 64, 128, and 500 TIP4P H_2O molecules.

III. Radial Structure of Water

Two well-known measures of liquid water's radial structure are the oxygen−oxygen radial distribution function, $g_{OO}(r)$, and the oxygen−hydrogen radial distribution function, $g_{OH}(r)$, Figures 1 and 2, respectively. As in subsequent sections, first, the functions predicted from the AIMD (BLYP/pw) simulations are presented. The physics contributing to structure is then examined by comparing several different empirical model predictions.

The structure of the first solvation shell is captured reasonably well by the AIMD (BLYP/pw) description of liquid water, as
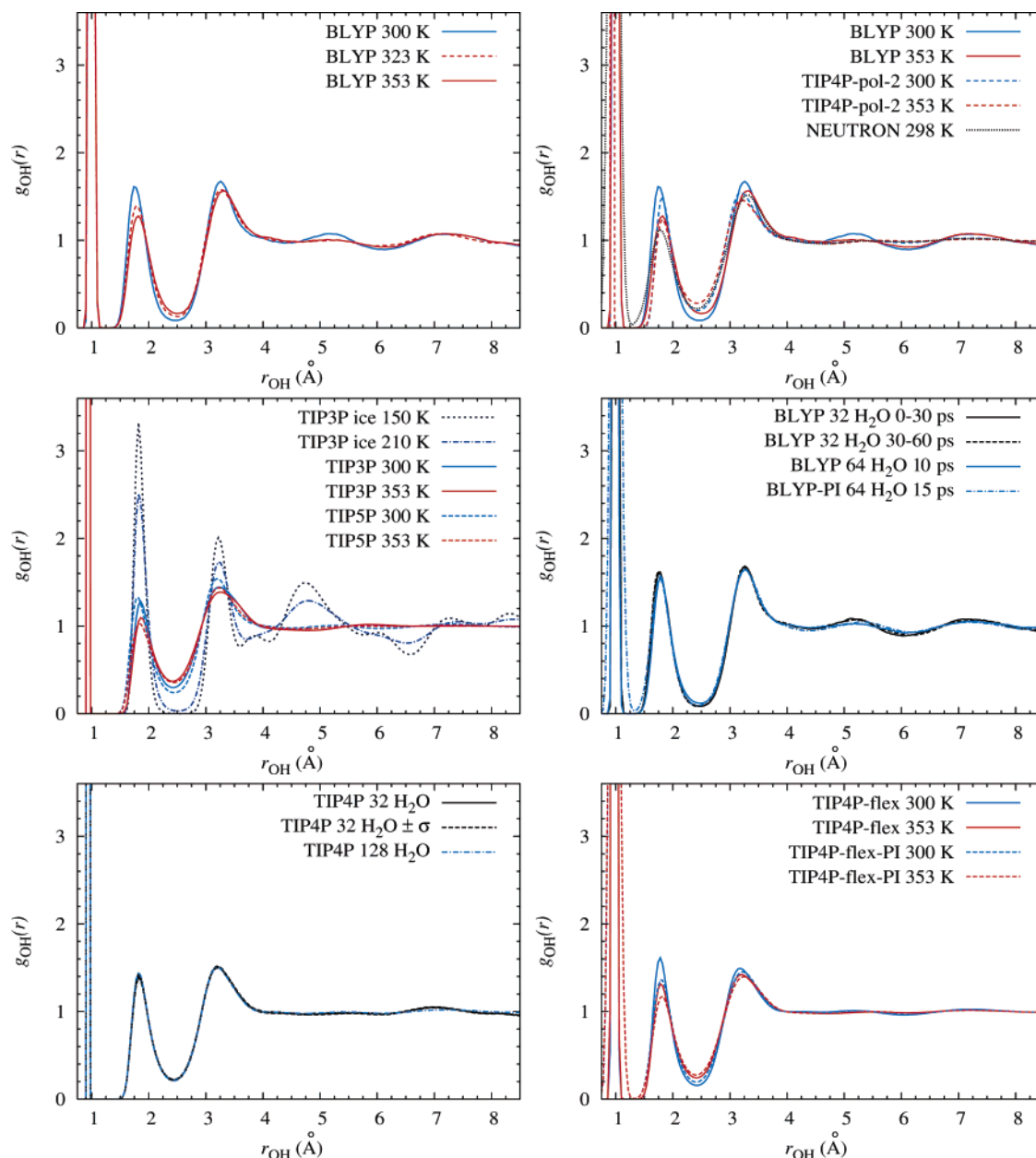
Structural Correlations and Motifs in Water

J. Phys. Chem. B, Vol. 110, No. 8, 2006 **3543**

Figure 2. Water and ice I_h $g_{OH}(r)$ values (0.04 Å bin). Neutron data from ref 5.

judged by comparison to results obtained from the TIP4P-pol-2 model,[12] which is able to reproduce X-ray scattering intensities from 275 to 350 K with high accuracy.[34] Thus, as suggested in ref 34, the radial structure predictions of TIP4P-pol-2 can be taken as a proxy for those[4,5] from diffraction experiments, which are obtained in reciprocal space and are also not yet available at all temperatures; however, the functions obtained from neutron diffraction data at 298 K[5] are also shown for comparison. The nearest-neighbor peaks of both $g_{OO}(r)$ and $g_{OH}(r)$ are somewhat higher in BLYP water compared to those of TIP4P-pol-2 water at 300 K, but this difference is less severe at higher temperatures. Furthermore, the outward shift of the peaks to larger r as the temperature is increased is captured by both models. Last, the predicted nearest-neighbor coordination numbers obtained by integrating the area under the first peak are similar (Table 2). Unfortunately, the BLYP description of the second solvation shell is overstructured compared to TIP4P-pol-2 or to the neutron data. In particular, the difference between

the first trough and second peak of $g_{OO}(r)$ is greatly enhanced, although the positions of these features are in excellent agreement.

The above discrepancies are attributed to deficiencies in the BLYP functional rather than to other potential sources of error.[35−40] For example, statistical error is insignificant: As shown in Figures 1 and 2, both $g_{OO}(r)$ and $g_{OH}(r)$ obtained by analyzing both 30 ps halves of the AIMD (BLYP/pw) trajectory at 300 K are essentially identical. Furthermore, the distance-dependent error bars calculated (section II) are nearly indistinguishable from the (mean) curve at the scale shown. Both tests are, thus, suggesting an effective sampling of local ordering, despite the fact that the dynamics are rather glassy, especially at 300 K, as reported by others[35] and confirmed here. Also, finite-size effects are inconsequential within the first shell and minor beyond: The $g(r)$ values predicted from a simulation with either 64 (not shown) or 128 TIP4P H_2O molecules are slightly shifted to larger r values beyond the first peak, while the functions from the AIMD (BLYP/pw) simulation with 64 H_2O

molecules (for 10 ps) are somewhat less structured but similar to those with 32 H_2O molecules; this effect is even more pronounced in the NVE ensemble.[33,35,37] Last, the radial structure is actually *enhanced* by inclusion of nuclear quantum effects due to the larger molecular dipole moment of AIPI (BLYP/pw) water, 3.18 ± 0.01 D,[30] compared to that of AIMD (BLYP/pw) water, about 3.04 D,[30,41−43] resulting from the stretching of the OH bond,[44] an effect that is not captured by empirical simulation models. Thus, this analysis is supporting recent work[35−40] arguing that BLYP water is intrinsically overstructured, a fact overlooked in earlier studies performed for much shorter periods of data collection but explained by the tendency of simple GGA-based functionals to overestimate the polarizability of molecules.[39] However, it is also possible that using a very large plane-wave cutoff, such as 160 Ry, may reduce the overstructuring. That is, the complete basis set limit has yet to be probed.

The current understanding of the physical "forces" affecting water's radial structure is confirmed by the present simulations. Although the first peak of $g_{OO}(r)$ is captured fairly well by the TIP3P model, the number of nearest neighbors is difficult to determine accurately (Table 2) because of the lack of structure beyond the first peak of $g_{OO}(r)$. On the basis of a comparison of the TIP4P and TIP5P models and as reported elsewhere,[16] the explicit treatment of lone pairs is helpful, but not essential, to predict correctly the radial structure beyond the first peak. Upon inclusion of quantum nuclei in the TIP4P-flex model, a slight (statistically significant) flattening of $g_{OO}(r)$ and a larger diminution of $g_{OH}(r)$ is observed. The latter effect is explained primarily by hydrogen atom tunneling into classically forbidden regions. Both changes are very similar to those noted in earlier calculations.[45,46] A molecule's average response at 300 K to the mean electric field of the other molecules is incorporated into the TIP4P model through its enhanced molecular dipole moment and, thus, both of its predicted functions are similar to those of the TIP4P-pol-2 model,[21] even at elevated temperatures. Last, by comparison of TIP4P versus TIP4P-flex results, both $g_{OO}(r)$ and $g_{OH}(r)$ are enhanced by a flexible monomer, in agreement with recent AIMD (BLYP/pw) simulations performed with both rigid and flexible H_2O molecules.[39]

IV. Spatial Structure of Water

The arrangement of a water molecule's neighbors in the liquid (or solid) is averaged out in the calculation of $g(r)$ but is effectively captured by the average oxygen and hydrogen spatial distributions[47] (Figures 3 and 4). The distribution of atom X's probability density about a water molecule (with its oxygen atom at the origin and oriented with the HOH plane parallel to the xz-plane) relative to the bulk density of atom X, $\rho_X(T)$, is labeled, $P_X(\mathbf{r};T)$, and is defined as follows

$$g_{OX}(r;T)4\pi r^2 = \int_{D(V)} P_X(\mathbf{r}';T)\delta(|\mathbf{r}'| - r)\,d\mathbf{r}'$$

$$\rho_X(T)\int_{D(V)} P_X(\mathbf{r};T)\,d\mathbf{r} = N - 1 \qquad (1)$$

The diagrams of the unitless function, $P_X(\mathbf{r};T)$, are easiest to interpret at short distances, because at large distances, the uniform fluid limit is recovered, i.e., $\lim_{|\mathbf{r}|\to\infty} P_X(\mathbf{r};T) = 1$. Accordingly, the spatial maps of both the first solvation shell (Figure 3) and the "interstitial" water molecules (Figure 4) defined as nontetrahedrally bonded water molecules at separations corresponding to the first minimum of $g_{OO}(r)$[47] are examined here. First, the functions predicted by AIMD (BLYP/pw) are compared to those of the TIP4P-pol-2 model, followed by a discussion of several different empirical model predictions.
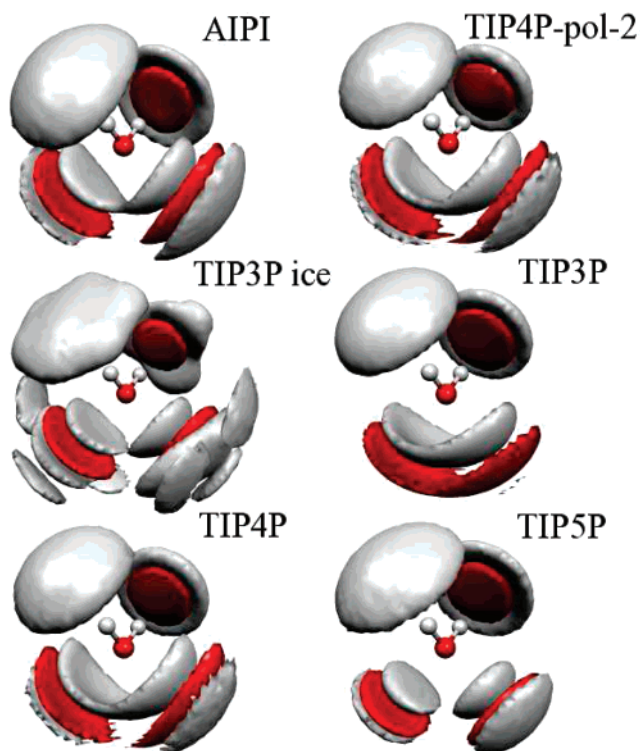

Figure 3. Nearest-neighbor distributions of oxygen (red) and hydrogen (gray) atoms in liquid water at 300 K and ice at 210 K. The enclosed regions have average oxygen or hydrogen densities at least 3.5 or 1.75 times greater, respectively, than that of the bulk. Equivalently, the isosurface values are $P_O(\mathbf{r}) = 3.5$ and $P_H(\mathbf{r}) = 1.75$.
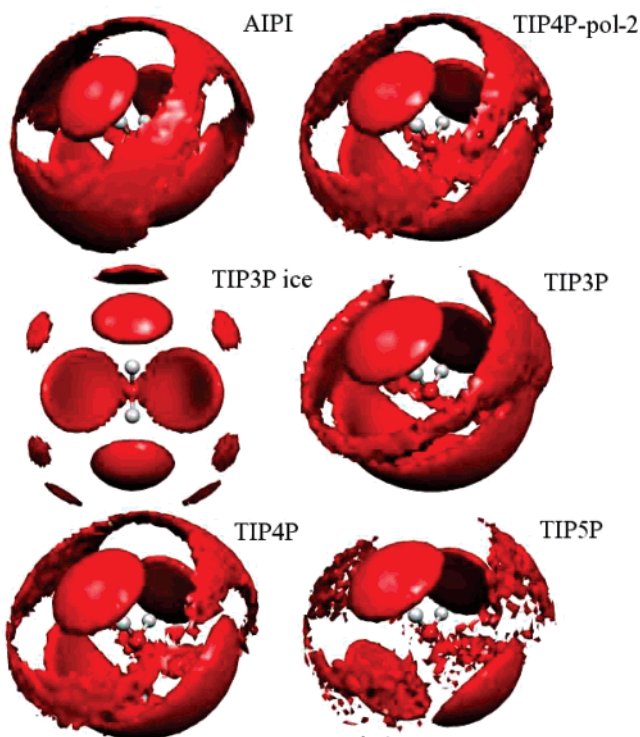

Figure 4. Nearest-neighbor and interstitial distributions of oxygen atoms in liquid water at 300 K and ice I_h at 180 K. The oxygen density of the enclosed regions is at least 1.4 times greater than that of the bulk. Equivalently, the isosurface value $P_O(\mathbf{r}) = 1.4$.

The first solvation shell structure is effectively captured by AIMD (BLYP/pw). In Figure 3, the oxygen atoms, in red, and the hydrogen atoms, in gray, of the nearest-neighboring water molecules in both AIPI (BLYP/pw) and TIP4P-pol-2 water are

Structural Correlations and Motifs in Water

J. Phys. Chem. B, Vol. 110, No. 8, 2006 **3545**

depicted. Note that the spatial distributions of the different ab initio models are very similar; however, those from the AIMD (BLYP/pw) simulation with 64 H_2O molecules (but a smaller $\mathcal{T} = 10$ ps) are noisier, while those from the simulations with 32 H_2O molecules are cluttered by additional molecules beyond the first shell due to finite-size effects, as suggested by the analysis of $g_{OO}(r)$. The agreement of the TIP4P-pol-2 and AIPI (BLYP/pw) isosurfaces is consistent with the similarity of the first peaks of their respective $g(r)$ values. The lobes depicting the two hydrogen-bond-accepting H_2O molecules in the upper hemisphere of the local frame of the central H_2O molecule are forced apart at the expected corners of a tetrahedron by the donating hydrogen atoms. However, the regions depicting the bonding hydrogen atoms of the two hydrogen-bond-donating H_2O molecules are more localized in the ab initio models compared to those in the TIP4P-pol-2 model because of the explicit treatment of the electron lone pairs on (the accepting) oxygen (atom). In Figure 4, the oxygen atoms of H_2O molecules both within the first shell and in interstitial or nontetrahedral positions between the first and the second solvation shells are shown. The TIP4P-pol-2 model is favoring interstitial positions in the upper hemisphere of the local frame, in agreement with earlier work;[47] the 64 H_2O AIPI (BLYP/pw) model is suffering from finite-size effects (based on tests performed) that are averaged out in the calculation of $g_{OO}(r)$.

The effect of certain model physics on these distributions is striking.[12] In Figure 3, a single cupped lobe denoting the oxygen atoms in TIP3P water is broken up into two diffuse caps in TIP4P water and distinct half-spheres in TIP5P water, whose donating hydrogen atoms are also highly localized. Thus, the (donor regions in the) spatial maps of the first shell structure are dramatically affected by the treatment of the oxygen atom's negative charge and by the presence of lone pairs. Incidentally, the outer hydrogen cloud for the hydrogen-bond donors in the TIP3P spatial map is nearly invisible at the (relative density) cutoff shown, 1.75, but forms caps with ill-defined edges like those of TIP4P at lower cutoff values, such as 1.6. In Figure 4, the nontetrahedral positions between the first and the second solvation shells are most populated in TIP3P water, followed by TIP4P and TIP4P-pol-2 water, and then TIP5P water and TIP3P ice I_h. The overestimation of interstitials in the TIP3P model is consistent with its lack of structure beyond the first peak of $g_{OO}(r)$. In contrast, the lone pairs of TIP5P water are not favorably situated for attracting H_2O molecules to nontetrahedral positions. Thus, the influence of the negative charge placement is acutely felt even beyond the first solvation shell. However, the distributions are largely unaffected by quantum delocalization of the donating hydrogen atoms,[12] inclusion of many-body polarizability effects (based on a comparison of the TIP4P-pol-2 and TIP4P maps), or a flexible versus constrained monomer. Additionally, their temperature dependence is weak,[12] marked by a slight decrease in the total enclosed isosurface volume at the high cutoffs shown (but an *increase* at smaller cutoffs).

V. Angular Structure of Water

The angular structure of liquid water is less well characterized due to the difficulty in obtaining experimental estimates.[6,48] Two important angles that are a direct probe of (the activation barrier to) orientational flexibility are the donor angle, $\alpha = \angle O_D-H_D\cdots O_A \approx 165°$ (Figure 5), and the acceptor angle, $\theta = \angle H_D\cdots O_A-H_A \approx 109.5°$ (Figure 6). Both angles are defined with respect to a donating (O_D-H_D) and accepting (O_A-H_A) molecule in the first solvation shell taken as the first intermolecular minimum of $g_{OH}(r)$, $r = 2.5$ Å (yielding essentially

identical results to a slightly different definition[12]). The results from the AIMD (BLYP/pw) simulations are discussed first, followed by the empirical model predictions.

The angular distribution of molecules in the first solvation shell is captured fairly well by the AIMD (BLYP/pw) description based on a comparison to the TIP4P-pol-2 model, which is able to reproduce quite accurately the inferred distribution of $\beta = \angle H_D-O_D\cdots O_A$ at 300 K,[12] the only angle for which experimental data is available.[6] The AIMD (BLYP/pw) distributions are slightly sharper than the empirical model's predictions, although they are still reconcilable with the amplitude of libration, 30°, thought to break hydrogen bonds.[49] Although their temperature dependence is not as uniform, the position of the maxima is similar at all temperatures and is consistent with a slightly bent hydrogen bond. The "overstructuring" of the AIMD (BLYP/pw) results is reminiscent of that afflicting both $g_{OO}(r)$ and $g_{OH}(r)$ and is attributed to deficiencies in the BLYP functional rather than to statistical error and/or finite-size effects based on arguments similar to those made in section III.

Interestingly, $P(\theta)$ is a more sensitive function of (certain) model physics than $P(\alpha)$. On the basis of a comparison of TIP3P or TIP4P versus TIP5P model results, $P(\alpha)$ is unaffected by the presence of TIP5P's pseudo-lone pairs, whereas $P(\theta)$ is markedly enhanced. These disparate observations are reconciled by reexamining the spatial maps (Figure 3), keeping in mind that they are drawn in a *local* reference frame and, thus, are depicting the average environment around every H_2O molecule in the system. Recall that the size and shape of the lobes in the *upper* hemisphere of the local frame are, both, relatively invariant to the choice of model. Thus, the coordinates of the O_A's in the relation defining α are nearly the same, and all three $P(\alpha)$'s, or equivalently $P(\beta)$'s in ref 12, are similar. Conversely, the spatial regions in the *lower* hemisphere of the local frame of Figure 3 are strikingly different, indicating that the instantaneous number and position of H_D atoms is more variable in the TIP3P and TIP4P models than in the TIP5P model, with a steep dimer energy profile.[16] Thus, $P(\theta)$ is enhanced in TIP5P water. The influence of other model physics on $P(\alpha)$ and $P(\theta)$ is similar to that on $g(r)$. Both TIP4P-flex distributions are broadened by a quantum treatment of nuclei, while the TIP4P distributions are just slightly enhanced by inclusion of molecular polarizability or a flexible monomer.

VI. Beyond "Traditional" Measures of the Solvent Shell: Joint Probability Density Functions

Several functions are already available to characterize simultaneously both the radial and orientational order in liquid water. The spherical harmonic expansion of the pair correlation function yields a "map" of the nearest neighbors[48] but carries a significant error due to the large number of terms required to describe the strongly directional intermolecular (hydrogen) bonds. The correlation function expansion of the entropy by a factorization of the N_{H_2O}-body correlation function[50] provides a simpler mathematical representation in terms of a few lower-dimensional functions. Another approach to probe structure is by analyzing restricted ranges of the angular space of the water dimer, $\Omega = (\omega_1, \omega_2)$, where $\omega = (\theta, \psi, \phi)$ are the Eulerian angles of a given molecule, to obtain restricted averages of the angular correlation function, $g(r, \omega_1, \omega_2)$,[51] and other (partially averaged) functions[52] that can now be precisely calculated. In this section, three-dimensional distribution functions, which have two independent variables and one dependent variable, are introduced as a new tool for analyzing liquid structure. Their evaluation is
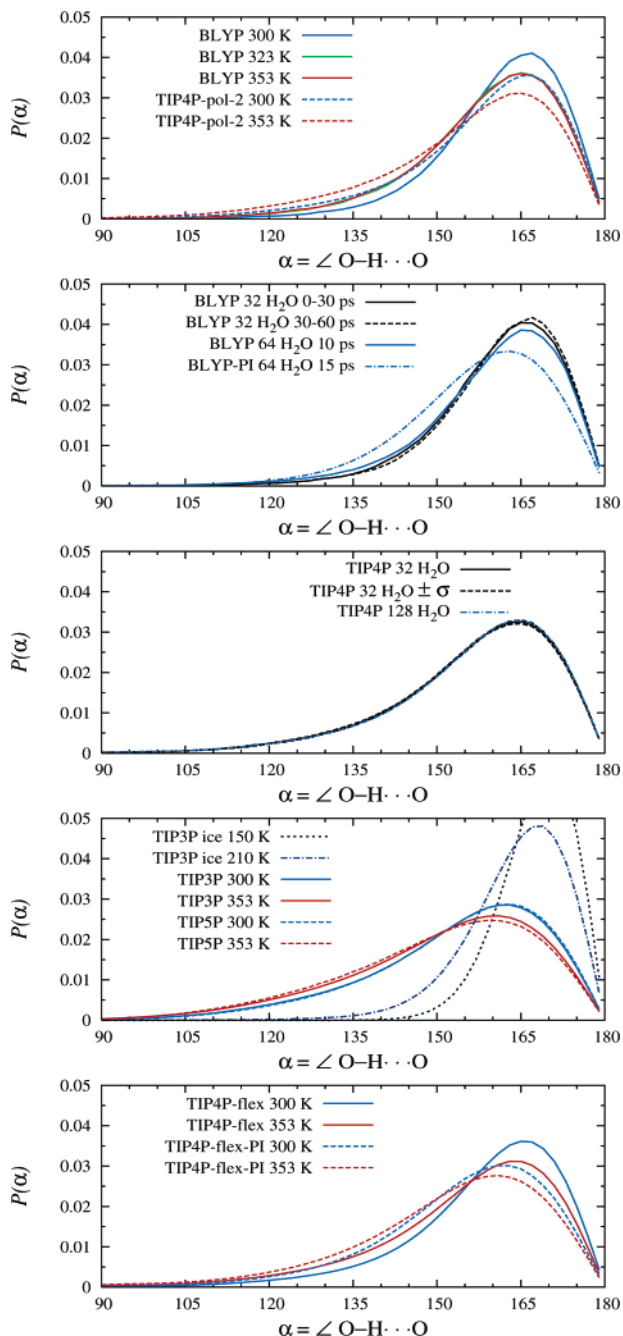
Figure 5. Water and ice I_h $P(\alpha)$ values (2° bin).

Figure 6. Water and ice I_h $P(\theta)$ values (2° bin).

then discussed for an idealized icelike cluster and for a rigid icelike lattice as a basis for understanding the structural predictions in ice I_h. Through the use of the most probable configurations identified in ice I_h, the functions obtained for liquid water are interpreted. Once again, the AIMD (BLYP/pw) and TIP4P-pol-2 functions are presented first, followed by a comparison of the TIPXP series of models.

It is useful to define three distribution functions with respect to a distance and common angles and torsions characterizing the water dimer. The first function, $g_2(r_{OH}, \cos(\alpha_{OHO}))$, is dependent on the distance, r_{OH}, between a hydrogen atom, H_D, and a not necessarily neighboring oxygen atom, O_A, and the cosine of the donor angle, $\alpha = \angle O_D - H_D \cdots O_A$. Because H_D and O_A might be separated by several angstroms, they do *not* always form a hydrogen bond. The second quantity, $g_2(r_{HO}, \cos(\theta_{HOH}))$, is defined similarly but with respect to the acceptor angle, $\theta = \angle H_D \cdots O_A - H_A$. In either case, the standard
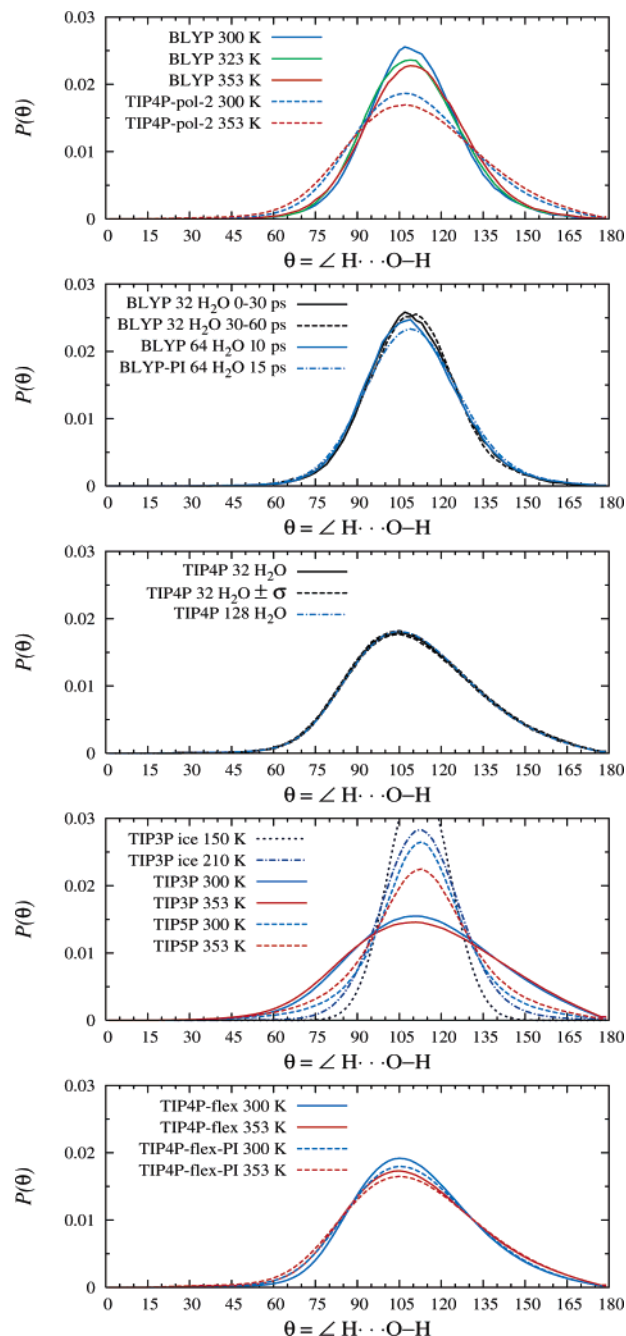
radial distribution function is recovered by integration

$$g(r;T) = \frac{1}{2} \int_{-1}^{1} g_2(r, \cos\theta;T) \, d(\cos\theta) \qquad (2)$$

In eq 2, the variable, $\cos\theta$, is employed to define the 3D distribution function as opposed to θ so that the distribution function, $g_2(r, \cos\theta;T)$, approaches unity at large radial distance without having to consider ill-conditioned Jacobian factors such as $\sin\theta$. In addition, a 3D radial–torsional distribution is probed, $g_2(r_{HO}, \omega_{HO_DH_D \cdots O_A})$, which is defined with respect to the dihedral angle formed between the covalent HO_D bond and the $H_D \cdots O_A$ axis when viewed along the second covalent O_DH_D bond. Once again, $g_{OH}(r)$ is recovered by integration

$$g(r;T) = \frac{1}{2\pi} \int_{-\pi}^{\pi} g_2(r, \omega;T) \, d\omega \qquad (3)$$

Structural Correlations and Motifs in Water

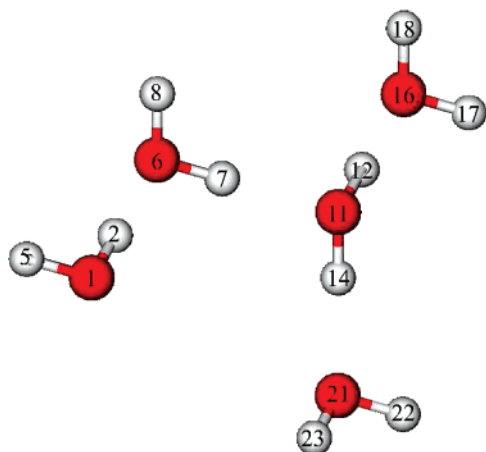*J. Phys. Chem. B, Vol. 110, No. 8, 2006* **3547**

Figure 7. Portion of an "idealized" ice I_h lattice with oxygen atoms separated by 2.768 Å in a perfectly symmetric (hexagonal) array, a fixed OH bond length of 0.993 Å, and a perfectly linear (donor angle, $\alpha = 180°$; acceptor angle, $\theta = 109.471°$) hydrogen bond.
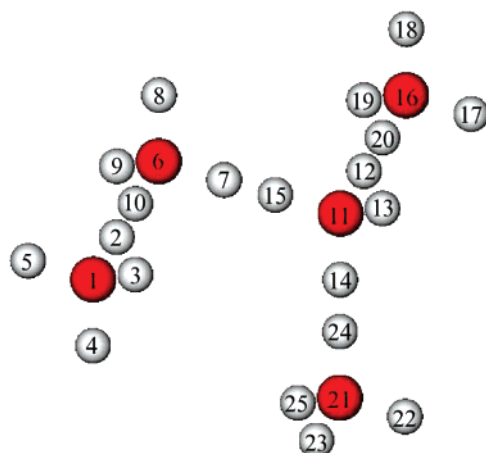

Figure 8. Illustration of the possible locations of the hydrogen atoms relative to the oxygen atoms O1, O6, O11, O16, and O21 in an "idealized" ice I_h lattice.

TABLE 3: Selected Groups of Either O−H−O or H−O−H Indices in Figure 8 with Certain Values of Either (r_{OH}, $\cos(\alpha_{OHO})$) or (r_{HO}, $\cos(\theta_{HOH})$), Respectively[a]

O−H−O	r_{OH} (Å)	$\cos \alpha$	H−O−H	r_{HO} (Å)	$\cos \theta$
1−2−1	0.993	1	2−1−2	0.993	1
1−2−6 (1a)	1.774	−1	2−1−3	0.993	−0.332
1−3−6 (1b)	3.239	0.591	2−6−7 (1α)	1.774	−0.332
1−2−11 (2a)	3.755	−0.718	2−1−7 (1β)	3.239	0.957
1−3−11 (2b)	4.630	0.215	3−1−7 (1γ)	3.239	−0.181
1−5−11 (2c)	5.365	0.874	3−1−9 (1δ)	3.239	−0.591
1−2−21 (3a)	4.858	−0.365	2−1−13 (2α)	4.630	0.726
1−3−21 (3b)	5.562	0.344	3−1−13 (2β)	4.630	0.215
1−5−21 (3c)	6.188	0.907	5−1−13 (2γ)	4.630	−0.869
1−2−16 (3d)	6.059	−0.902	2−1−12 (2δ)	5.365	0.874
1−3−16 (3e)	7.169	0.267	5−1−12 (2ε)	5.365	−0.750
1−5−16 (3f)	7.665	0.732	2−1−20 (3α)	6.059	0.903

[a] The group labels are in parentheses.

For a randomly selected group of water molecules (Figure 7) excised from an idealized, proton-disordered ice I_h lattice, the three functions defined above are easily interpreted. The independent variables of these functions are determined by calculating the distances and angles for every different combination of atoms, either O−H−O, H−O−H, or H−O−H−O, in Figure 7. For example, the coordinates of the selected atom combinations O−H−O = 1−2−11, H−O−H = 2−1−8, and H−O−H−O = 5−1−2−6 are (r_{OH}, $\cos \alpha$) = (3.755 Å, −0.718), (r_{HO}, $\cos \theta$) = (3.239 Å, 0.957), and (r_{HO}, ω) = (1.774
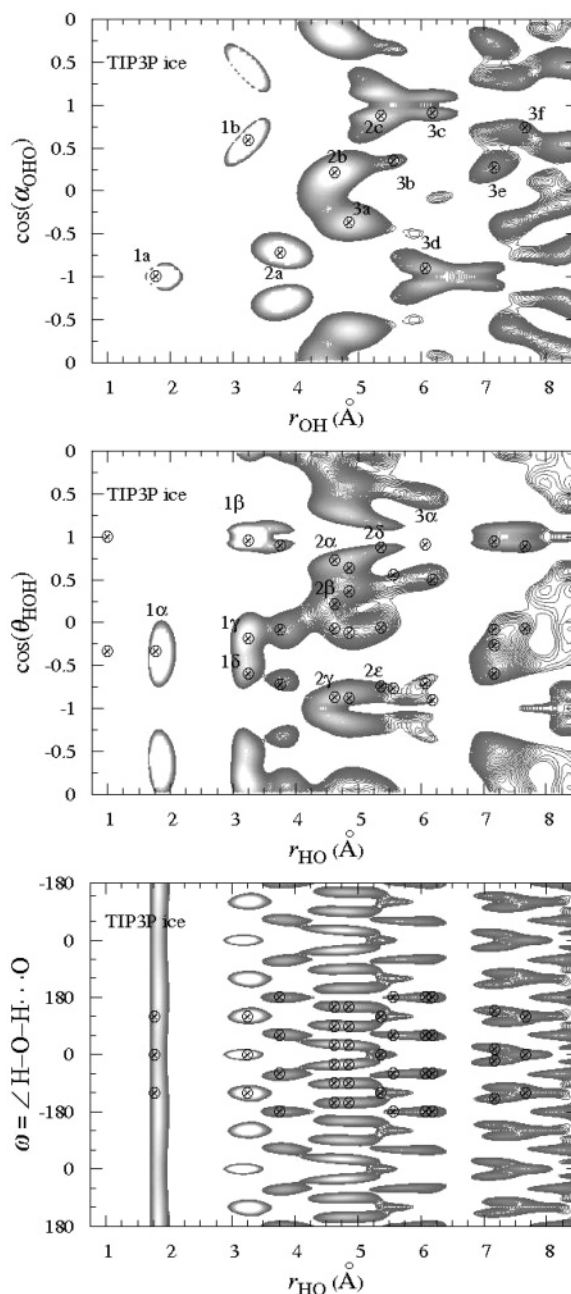

Figure 9. $g_2(r_{OH},\cos(\alpha_{OHO}))$ (top), $g_2(r_{HO},\cos(\theta_{HOH}))$ (middle), and g_2-($r_{HO},\omega_{HO_DH_D\cdots O_A}$) (bottom) contour plots of TIP3P ice I_h at 150 K. Only contour lines ranging above 1.05 are shown, and the circled crosses are structures taken from "idealized" clusters, Figure 8, as discussed in the text.

Å, 120°), respectively, yielding nonzero values of their respective functions.

The 3D joint distribution functions of ice I_h are effectively generated by sampling all of the possible clusters, such as Figure 7, comprising ice I_h. Therefore, to interpret the 3D joint distribution functions of ice I_h, a *fictitious* model system is constructed, Figure 8, with four dummy (hydrogen) atoms placed around every oxygen atom at the corners or apexes of a tetrahedron. All of the values of either (r_{OH}, $\cos \alpha$), (r_{HO}, $\cos \theta$), or (r_{HO}, ω) that are possible between a molecule and its nearest neighbor, second-nearest neighbor, and third-nearest neighbors in Figure 8 are straightforwardly determined by systematically calculating the distances and angles for every combination of atoms, either O−H−O, H−O−H, or H−O−H−O, respectively. The configurations that are "allowed" in
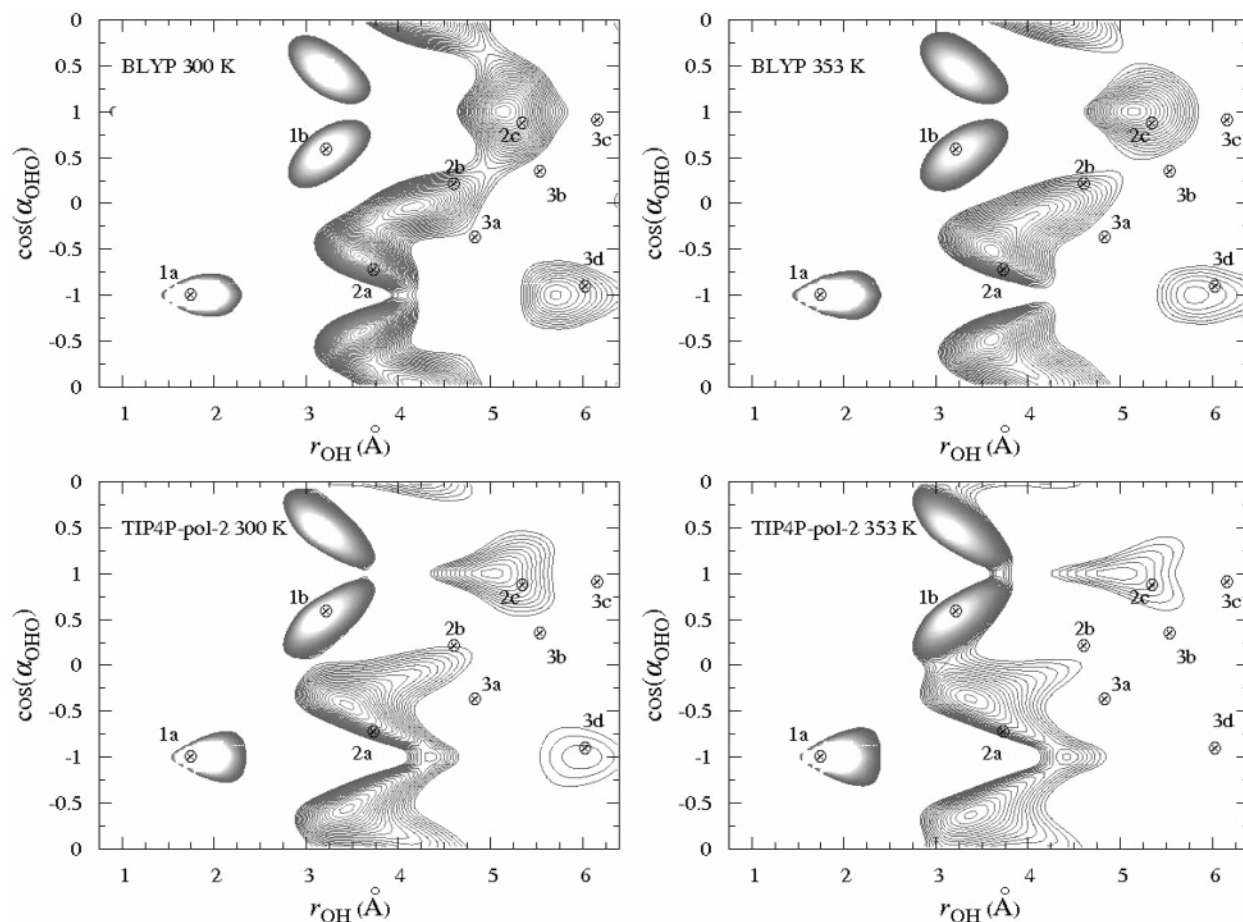
Figure 10. $g_2(r_{OH},\cos(\alpha_{OHO}))$ contour maps of BLYP water at 300 and 353 K and TIP4P-pol-2 water at 300 and 353 K. Refer to the caption of Figure 9 for additional details.
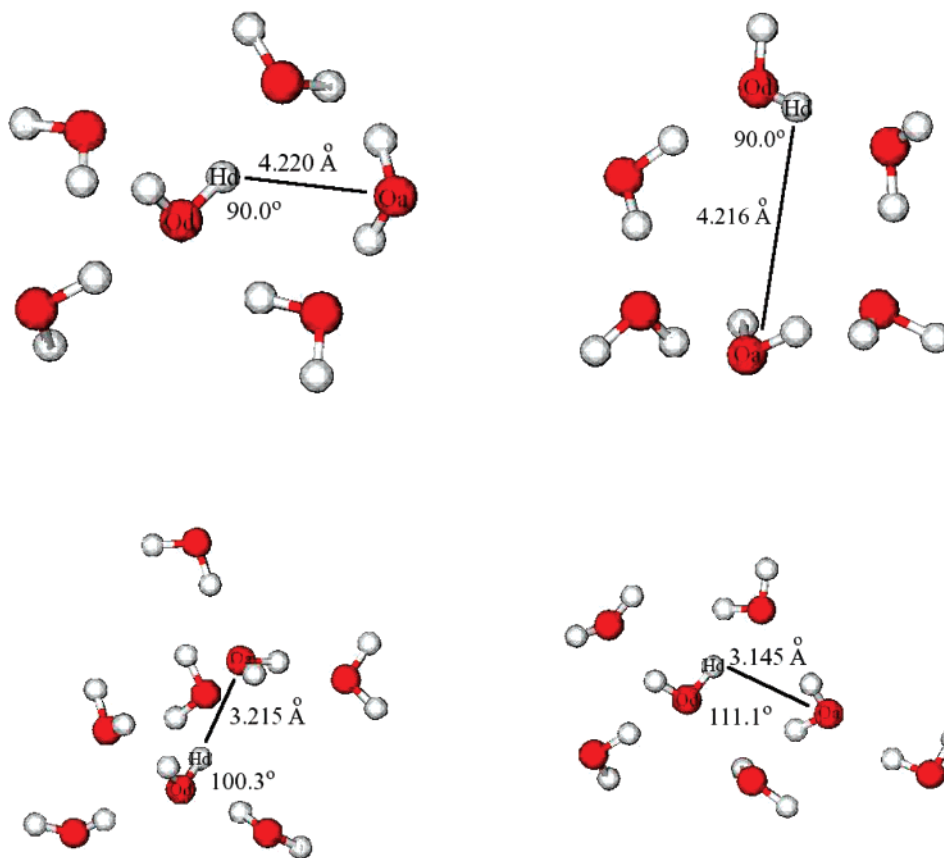

Figure 11. Snapshots from the AIMD (BLYP/pw) (top) and TIP4P-pol-2 (bottom) liquid water simulations at 300 K with selected molecules shown.
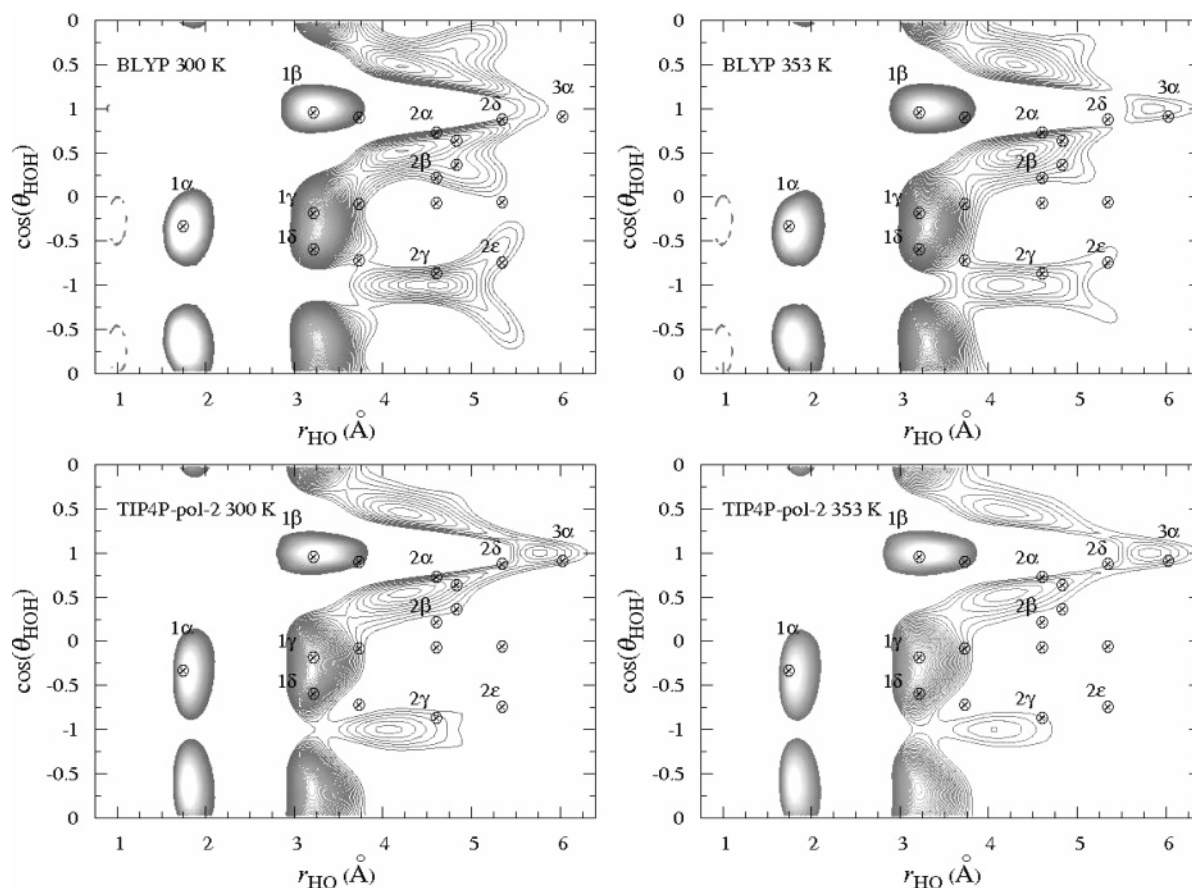
Structural Correlations and Motifs in Water

J. Phys. Chem. B, Vol. 110, No. 8, 2006 **3549**

Figure 12. $g_2(r_{HO}, \cos(\theta_{HOH}))$ contour maps of BLYP water at 300 and 353 K and TIP4P-pol-2 water at 300 and 353 K. Refer to the caption of Figure 9 for additional details.

ice I_h are those with one hydrogen atom between adjacent oxygens (i.e., satisfying the Bernal−Fowler ice rules). For example, an ice I_h lattice with adjacent H_2O molecules that have the H−O−H combinations (or apical numbers) 2−6−7, 2−6−8, or 2−6−9 is allowed, but a structure with atoms 2−6−10 is forbidden because of the juxtaposition of atoms 2 and 10. Note that these allowed H−O−H combinations are degenerate, i.e., have identical values of $(r_{HO}, \cos \theta) = (1.774$ Å, $-0.332)$ in the model system, so the value of $g_2(1.774$ Å, $-0.332)$ is expected to be large in ice I_h.

Through the use of Figure 8, the joint distribution functions of hexagonal ice I_h, Figure 9, are more easily understood. The various combinations of apical numbers in Figure 8 that are "allowed" in ice I_h are labeled as circled crosses in the corresponding contour plot of TIP3P ice I_h (Figure 9). Every circled cross is centered atop or near a local maximum in Figure 9, denoted by a lighter (versus darker) region. The only "exception" is point 3α, which is, in fact, a local maximum at smaller contour values. Thus, the major features in the contour plots of ice I_h can each be assigned to a unique combination of atoms in Figure 8. The peculiar shape of the contour regions is attributed to the thermal disordering or "scrambling" of these icelike configurations. In fact, "dimers" that are close to each other in the coordinate space of Figure 8 are overlapping in the top, middle, and bottom panels of Figure 9 over the range of z-values shown. The coordinates of some of these "allowed" combinations are given in Table 3 and are designated by solvation shell (i.e., 1, 2, ...) and atom group (i.e., Roman letters for O−H−O and Greek letters for H−O−H). For example, the circled cross labeled 1b in the top panel of Figure 9 designates the atom group O−H−O = 1−3−6, while 2β in the middle panel corresponds to H−O−H = 3−1−13. Note that each point

is matched to a solvation shell by inspection of $g_{OH}(r)$, Figure 2; also, peaks within the same shell have a similar density of contour lines.

The size, shape, and intensity of the neat liquid water contours can also be explained using Figure 8. In the contour plots of the $g_2(r_{OH}, \cos(\alpha_{OHO}))$ function predicted by AIMD (BLYP/pw) (Figure 10), nearly every maximum is situated near a circled cross at both 300 and 353 K. The first solvation shell maxima labeled by points 1a and 1b are attributed to atom groups O−H−O = 1−2−6 and O−H−O = 1−3−6, respectively, in Figure 8 (and other degenerate combinations, e.g., 6−7−11 and 1−4−6). The second solvation shell, denoted by a thick, continuous gray band, includes points 2a, represented by atoms 1−2−11 in Figure 8, 2b (1−3−11), and 2c (1−5−11). A weak third-shell feature is present near point 3d. The maximum at (4.22 Å, 0) that is located relatively far from any circled crosses consists, in fact, of two types of distorted icelike configurations resembling 2b and 3a, based on the systematic inspection of many "snapshots" with the specified geometric parameters taken from the simulation, two of which are shown in Figure 11. As the temperature is increased, the peaks observed at 300 K are less pronounced or disappear altogether at 353 K, while the contours are "attracted" or pulled toward the circled crosses no longer near a maximum. However, the positions of the remaining maxima are relatively unchanged.

Consistent with other measures examined, TIP4P-pol-2 water is relatively less ordered than that of AIMD (BLYP/pw); interestingly, the contour plot of TIP4P-pol-2 water at 300 K resembles more closely that of BLYP water at 353 K than at 300 K (Figure 10), with some important differences. First, a second maximum is present at (4.34 Å, −1) in the TIP4P-pol-2 contour at 300 K, accompanying that at (3.46 Å, −0.425), which
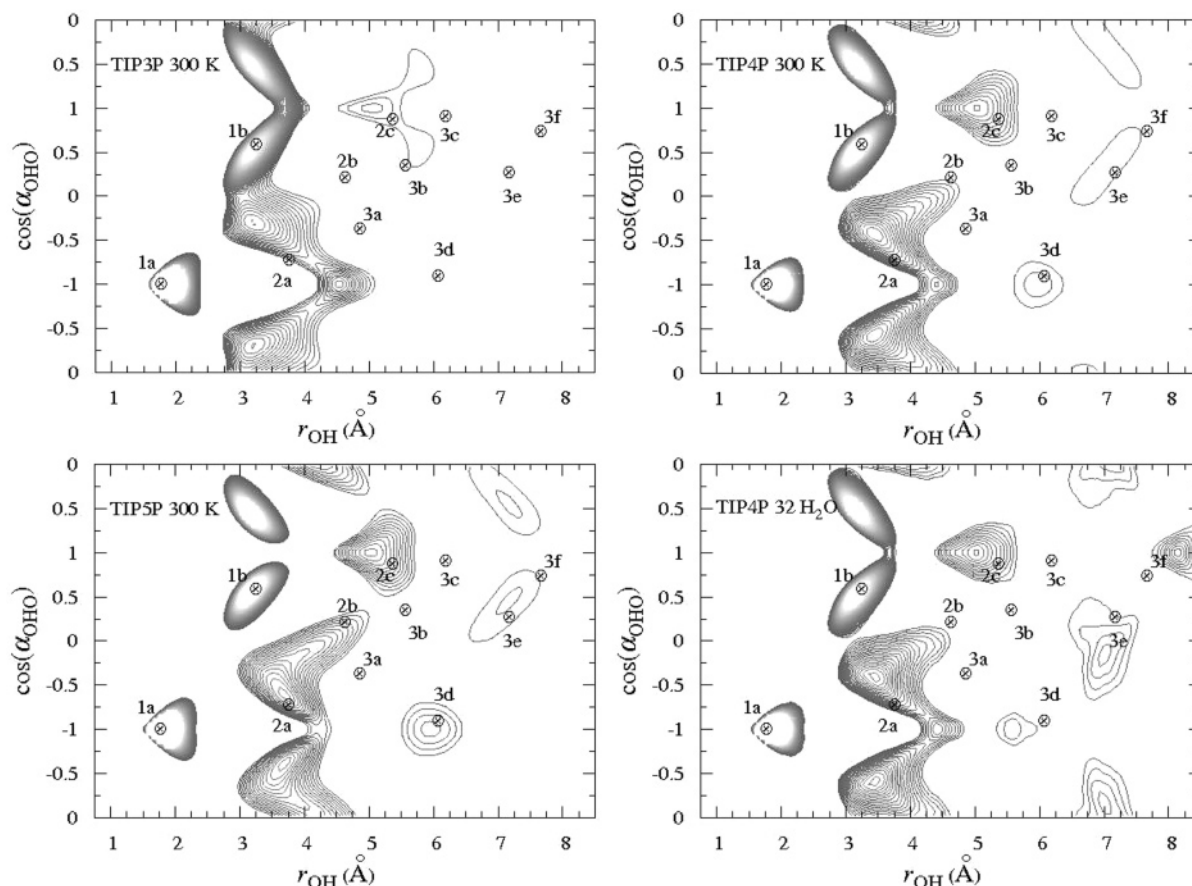
Figure 13. $g_2(r_{OH}, \cos(\alpha_{OHO}))$ contour maps of TIP3P, TIP4P, and TIP5P water at 300 K and that of a TIP4P run with AIMD (BLYP/pw) simulation parameters. Refer to the caption of Figure 9 for additional details.

is relatively far from 2a. On the basis of an examination of "snapshots", both of these maxima are comprised largely of structures resembling 2a and a small fraction of distorted third-shell configurations, especially at 4.34 Å. The edge of the contour lines extending from roughly (3.0 Å, 0) to 2b is, also, shaped differently, perhaps due to the influence of the interstitial H_2O molecules. The $(r_{OH}, \cos(\alpha_{OHO}))$ coordinates in the TIP4P-pol-2 spatial diagram, Figure 4, where interstitials are most pronounced are (3.21 Å, −0.18) in the upper hemisphere of the local frame and either (3.14 Å, −0.36) or (4.50 Å, 0.96) (depending on the central H_2O molecule's H_D) in the lower hemisphere. Representative "snapshots" of an interstitial H_2O molecule in both hemispheres of the local frame are shown in Figure 11. As suggested by the figure, the interstitial H_2O molecules are not typically "free" H_2O molecules occupying a void in an icelike lattice (although this is statistically possible), but rather they themselves are part of a distorted hydrogen-bond network.

The overstructuring of AIMD (BLYP/pw) water compared to TIP4P-pol-2 water is also observed in the contour plots of $g_2(r_{HO}, \cos(\theta_{HOH}))$ (Figure 12). The sharpest (unlabeled) features in the BLYP contours at $r_{HO} \approx 1.0$ Å are assigned to the intramolecular atom combinations, H−O−H = 2−1−2 or H−O−H = 2−1−3. Both models are correctly predicting four sharp peaks, 1α−1δ, in the first solvation shell represented by the icelike configurations, 2−6−7, 2−1−7, 3−1−7, and 3−1−9, respectively (Table 3). Two of these peaks (1α and 1β) are comprised of several possible "degenerate" combinations of atoms and, thus, are quite intense. Beyond the first solvation shell, the long, diagonal contour beginning at (∼3.75 Å, 0.25) and ending at (∼5.75 Å, 1) and traced by the points 2α, 2β, and 3α, which are the ice I_h structures 2−1−13, 3−1−13, and

2−1−20, respectively, is noticeably "thicker" in BLYP water. Thus, over the range of z-values shown, AIMD (BLYP/pw) is clearly overstructured in the second solvation shell compared to the TIP4P-pol-2 model, which is consistent with the $g_{OH}(r)$ values obtained.

Insight into the intermediate- and long-range structure of liquid water, and the effect of model physics, is gleaned by inspection of the contour plots of $g_2(r_{OH}, \cos(\alpha_{OHO}))$ obtained from the TIP3P, TIP4P, and TIP5P models (Figure 13). As expected, TIP3P is understructured, while TIP5P is the most icelike. The maxima in the TIP3P contour plot are located far from the circled crosses; however, this does not necessarily imply a mixture of configurations. For example, the maximum at (3.18 Å, −0.275) is comprised nearly exclusively of configurations resembling 2a (Figure 14, top panel) and *not* 1b, which would require a prohibitive distortion of the nearest-neighbor hydrogen-bond angle, α, while the point (4.54 Å, −1.0) consists of a mixture of highly distorted 2a and 3a structures (Figure 14, middle and bottom panels), based on an examination of the TIP3P trajectory. In addition, the contours describing TIP3P's second solvation shell are less dense than those of any other model examined. The icelike configurations responsible for the third-shell structure in either TIP4P or TIP5P water are denoted by the circled crosses, 3d (1−2−16), 3e (1−3−16), and 3f (1−5−16). Interestingly, the contribution from the (diagonal of) points 3a−3c in Figures 10 and 13, represented by atom groups, 1−2−21, 1−3−21, and 1−5−21, is not quite as significant (as seen by reducing the minimum contour value). One hypothesis is that a "linear" (tetrameric) chain of water molecules (consisting of oxygen atoms O1, O6, O11, and O16) is, on average, slightly more probable than a "bent" chain (substituting O21 for O16), perhaps due to the favorable
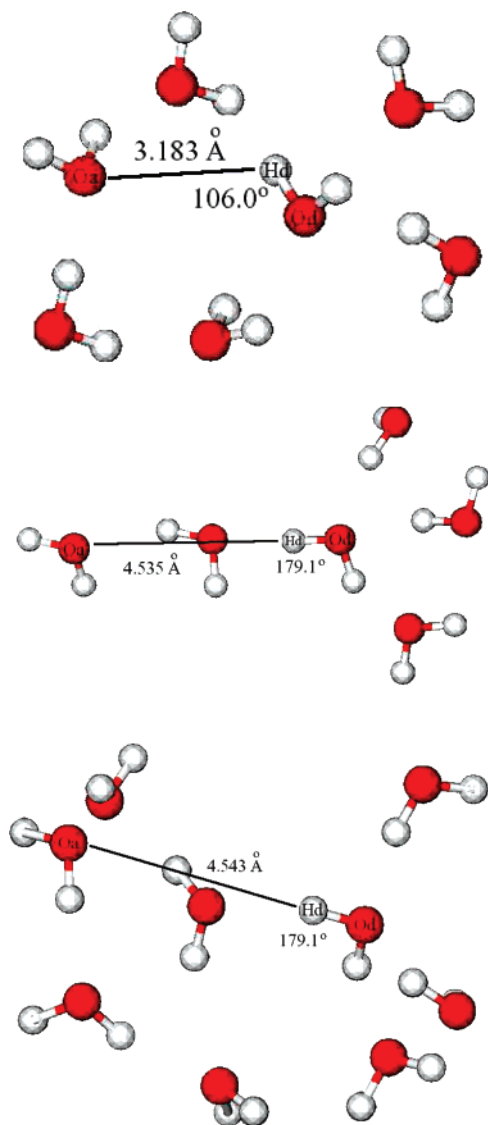
Figure 14. Snapshots from the TIP3P liquid water simulation at 300 K with selected molecules shown.

orientation of the H_2O molecular dipole moments. The contours of the other empirical models with different physics included (i.e., TIP4P-flex, TIP4P-flex-PI, TIP4P-pol-2) are all roughly similar to that of TIP4P. Both statistical uncertainty and finite-size effects in the AIMD (BLYP/pw) contour plots are estimated by comparing the 128 molecule TIP4P results to those obtained from a TIP4P water simulation performed with 32 H_2O molecules for $\mathcal{T} = 60$ ps (Figure 13). The predicted maps are quite consistent, except for spurious (finite-size) effects beyond the second solvation shell (>6 Å).

These same conclusions are reached by examining $g_2(r_{HO},\cos(\theta_{HOH}))$, but within the first solvation shell, this measure is even more dependent on the model physics. The sensitivity of θ (as opposed to α) on the charge placement, first revealed by the analysis of $P(\theta)$ (Figure 6), is substantiated by the shape of the peak underneath point 1α in Figure 15, which is confined to a narrower range of θ values in TIP5P water than in either TIP3P or TIP4P water. In addition, the TIP3P maximum near point 1β is shifted to slightly larger r_{OH} distances due to a weaker hydrogen bond. Like other measures examined, these maps are less sensitive to other changes in the model physics, while statistical error is minor, and finite-size effects are negligible for values of $r_{HO} \leq 6$ Å.

The treatment of the water hydrogen bond by the different theoretical models is clarified further by an analysis of the final measure, $g_2(r_{HO},\omega_{HO_DH_D\cdots O_A})$ (Figure 16). The probability distribution of the dihedral angle, $\omega_{HO_DH_D\cdots O_A}$, characterizing the water dimer is only slightly depressed near (1.77 Å, 0°) in TIP3P ice I_h, but it is noticeably peaked at $\omega = 0°$ in TIP3P water. In an idealized ice lattice with a bent hydrogen bond, five values of $\omega_{HO_DH_D\cdots O_A}$ at $r_{HO} \approx 1.77$ Å are feasible, 0° (3−1−2−6 in Figure 8), ±120° (either 4−1−2−6 or 5−1−2−6 in Figure 8), and ±180° (3−1−2−6 if $\alpha \neq 180°$). Apparently, however, these spikes are flattened in either ice I_h or liquid water by the nearly isoenergetic rotation of H_D in a cone about O_A. The "cone effect" is enhanced in ice I_h due to its larger (mean) hydrogen-bond angle, α (Figure 5). Furthermore, it is a purely classical phenomenon; the distributions predicted by AIPI and AIMD (BLYP/pw) water are quite similar. Indeed, in liquid water, these distributions are affected mostly by the molecular distribution or placement of charge, as described for the first solvation shell in a prior publication.[12]

Other differences between TIP3P ice (Figure 9) and liquid water that are probed by this measure are also of interest. Of the three sharp peaks at $r_{HO} \approx 3.24$ Å in ice I_h, represented by the atom combinations 2−1−3−6, 4−1−3−6, and 5−1−3−6 in Figure 8, two of them (i.e., 4−1−3−6 and 5−1−3−6) are flattened considerably in liquid water, indicating that the donating H_2O molecule is relatively "free" to rotate about its hydrogen bond and not constrained by its neighbors, as in a lattice network. The only remaining features of note in the TIP3P surface plot are two ridges with maxima matched to the atom combinations 3−1−2−11 (3.76 Å, 60°) and 4−1−2−11 (3.76 Å, −60°) and a weak feature at $r_{HO} \approx 5.75$ Å assigned to 2−1−5−11 (5.37 Å, 0°). Note that some differences are observed between the plots of TIP3P and those of the other models, along with a slight temperature dependence, but the major features are similar.

VII. Conclusions

Both "traditional" and novel measures of water structure are examined for a series of increasingly realistic theoretical models ranging from TIP3P to a fully ab initio (BLYP/pw 80 Ry) treatment with quantum nuclei. The findings here are supporting the emerging consensus in the literature that AIMD (BLYP/pw 70−85 Ry) and TIP5P water are somewhat overstructured, whereas TIP4P-pol-2 water provides an excellent description of structural properties. In addition, new three-dimensional joint distribution functions are used to identify common structural motifs predicted by the different theoretical models. The general conclusion from the analysis of these functions is that the most prevalent structures in liquid water are thermally disordered clusters derived from the (proton-disordered) hexagonal ice lattice.

Thus, all of the calculated quantities are reconcilable with a tetrahedral arrangement of the H_2O molecules in the first solvation shell. Irrespective of model, the coordination number that is calculated from models with a well-defined first minimum of $g(r)$ is about four, the spatial maps of the first solvation shell are explained by a fourfold coordinated H_2O molecule, the angular distribution function is peaked at the tetrahedral angle, and short-, intermediate-, and long-range correlations in the new three-dimensional joint distribution functions examined here are successfully assigned based on configurations taken from an ice I_h lattice. The consistency of these predictions from theoretical models whose physics is quite different is compelling evidence in favor of a traditional model of this complex fluid.
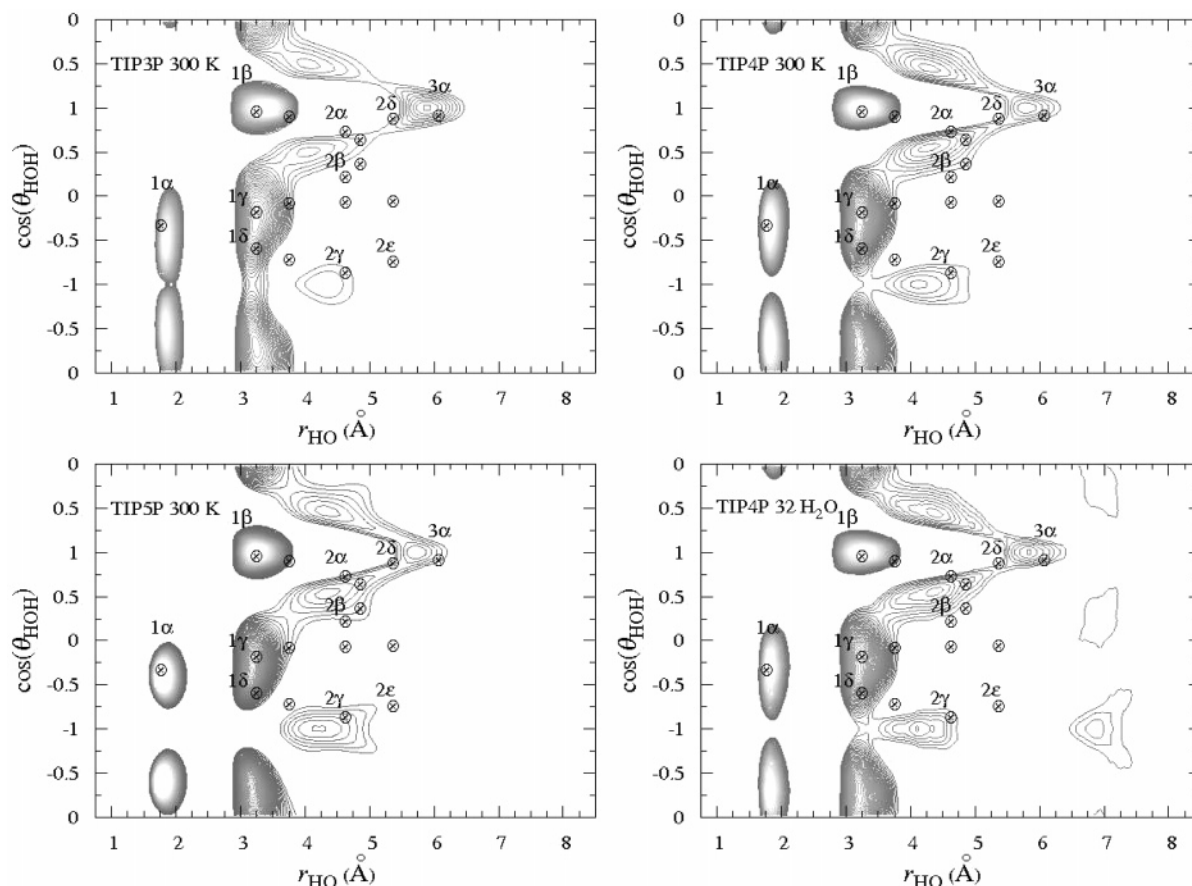
Figure 15. $g_2(r_{HO}, \cos(\theta_{HOH}))$ contour maps of TIP3P, TIP4P, and TIP5P water at 300 K and that of a TIP4P run with AIMD (BLYP/pw) simulation parameters. Refer to the caption of Figure 9 for additional details.

Appendix A: Path-Integral Studies of a TIP3P- and TIP4P-flex H$_2$O Molecule

The choice of simulation parameters for the path-integral study of TIP4P-flex water is made by performing several tractable tests with a single H$_2$O molecule. First, the optimum number of beads, P,[30] is selected by converging the (intramolecular) potential energy of a TIP3P-flex H$_2$O molecule with (CHARMM) harmonic bonds and bends.[55] This energy is expected to be a linear function of $1/P^2$ for large P. (Note that the constant kinetic energy contribution of $^3/_2NkT$ has been subtracted out.) From the results of several sufficiently long ($\mathcal{T} = 100$ ps) path-integral simulations of a single TIP3P-flex monomer at 300 K and with varying numbers of beads, P, but a fixed time step, $\delta t = 1$ fs, the (intramolecular) potential energy can be plotted as a function of $1/P^2$ (Figure 17). For $P > 8$, the plot is approximately linear, as expected. The increase in energy observed upon doubling P from 32 to 64 is 0.16 kcal/mol, from 64 to 128 is 0.05 kcal/mol, and from 128 to 256 is 0.09 kcal/mol (larger due to statistical error). Thus, a value of $P = 64$ is a reasonable choice for modeling the liquid, especially considering that the energy of the monomer is dominated by contributions from high-frequency (bending and stretching) modes, which are most sensitive to the choice of P.

After P was selected based on the potential energy of a molecule which is equivalent to converging the equilibrium OH bond length and $\angle$HOH angle, a second test is performed to verify δt. The quantum kinetic energy of the beads, a component of the total energy, is calculated by two methods, labeled primitive[56] (prim) and virial[57] (vir), that converge as either the simulation length is increased or the time step is decreased. The difference between these quantities is estimated as a function of δt by performing five successive 100 ps simulations and calculating the mean (over 500 ps) of each quantity and a sample standard deviation, $\pm s$ (based on five 100 ps values). The difference between these two energies is small for $\delta t = 1$ fs and essentially zero for $\delta t < 0.5$ fs (Table 4). Thus, $\delta t = 0.5$ fs would be ideal for studying the neat liquid, but $\delta t = 1$ fs would also suffice.

The final test is a verification that the parameters chosen are applicable to a TIP4P-flex monomer as well. Three 100 ps simulations are performed of a TIP4P-flex H$_2$O molecule at 300 K with $P = 32$, 64, and 128 beads and $\delta t = 0.5$ fs. The increase in energy observed upon doubling P from 32 to 64 is 0.17 kcal/mol and from 64 to 128 is 0.03 kcal/mol (Figure 17), very similar to the TIP3P-flex monomer. In addition, the difference, $\langle \text{vir} \rangle - \langle \text{prim} \rangle$, is acceptably small but growing as P is increased
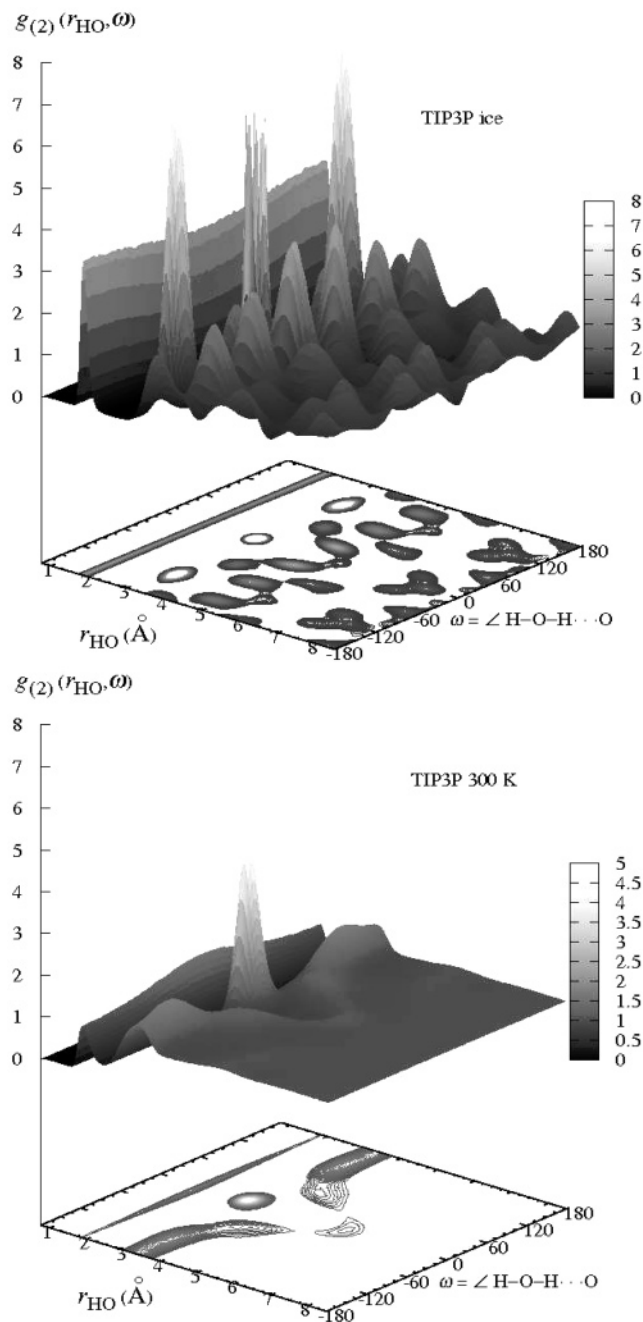
Structural Correlations and Motifs in Water

J. Phys. Chem. B, Vol. 110, No. 8, 2006 **3553**

TABLE 4: Convergence of Prim and Vir Kinetic Energy (KE), Units 10^{-5} a.u.

	δt		
	1 fs	0.5 fs	0.25 fs
$\langle$prim KE$\rangle \pm s$	1225 ± 4	1231 ± 2	1228 ± 3
$\langle$vir KE$\rangle \pm s$	1238 ± 1	1234 ± 1	1233 ± 1

References and Notes

(1) Errington, J. R.; Debenedetti, P. G. *Nature* **2001**, *409*, 318

(2) Narten, A. H.; Levy, H. A. *J. Chem. Phys.* **1971**, *55*, 2263. Soper, A. K.; Phillips, M. G. *Chem. Phys.* **1986**, *107*, 47.

(3) Barker, J. A.; Watts, R. *Chem. Phys. Lett.* **1969**, *3*, 144. Rahman, A.; Stillinger, F. H. *J. Chem. Phys.* **1971**, *55*, 3336. Stillinger, F. H.; David, C. W. *J. Chem. Phys.* **1978**, *69*, 1473. Kuharski, R. A.; Rossky, P. J. *J. Chem. Phys.* **1985**, *82*, 5164. Laasonen, K.; Sprik, M.; Parrinello, M.; Car, R. *J. Chem. Phys.* **1993**, *99*, 9080.

(4) Hura, G.; Sorenson, J. M.; Glaeser, R. M.; Head-Gordon, T. *J. Chem. Phys.* **2000**, *113*, 9140.

(5) Soper, A. K. *Chem. Phys.* **2000**, *258*, 121.

(6) Modig, K.; Pfrommer, B. G.; Halle, B. *Phys. Rev. Lett.* **2003**, *90*, 075502.

(7) Wernet, Ph.; Nordlund, D.; Bergmann, U.; Cavalleri, M.; Odelius, M.; Ogasawara, H.; Näslund, L.-Å.; Hirsch, T. K.; Ojamäe, L.; Glatzel, P.; Pettersson, L. G. M.; Nilsson, A. *Science* **2004**, *304*, 995.

(8) Smith, J. D.; Cappa, C. D.; Wilson, K. R.; Messer, B. M.; Cohen, R. C.; Saykally, R. J. *Science* **2004**, *306*, 851.

(9) Nilsson, A.; Wernet, Ph.; Nordlund, D.; Bergmann, U.; Cavalleri, M.; Odelius, M.; Ogasawara, H.; Näslund, L.-A.; Hirsch, T. K.; Ojamäe, L.; Glatzel, P.; Pettersson, L. G. M. *Science* **2005**, *308*, 793a.

(10) Smith, J. D.; Cappa, C. D.; Messer, B. M.; Cohen, R. C.; Saykally, R. J. *Science* **2005**, *308*, 793b.

(11) Näslund, L.-Å.; Lüning, J.; Ufuktepe, Y.; Ogasawara, H.; Wernet, Ph.; Bergmann, U.; Pettersson, L. G. M.; Nilsson, A. *J. Phys. Chem. B* **2005**, *109*, 13835.

(12) Mantz, Y. A.; Chen, B.; Martyna, G. J. *Chem. Phys. Lett.* **2005**, *405*, 294.

(13) Car, R.; Parrinello, M. *Phys. Rev. Lett.* **1985**, *55*, 2471.

(14) Iftimie, R.; Minary, P.; Tuckerman, M. E. *Proc. Natl. Acad. Sci. U.S.A.* **2005**, *102*, 6654.

(15) Jorgensen, W. L.; Chandrasekhar, J.; Madura, J. D.; Impey, R. W.; Klein, M. L. *J. Chem. Phys.* **1983**, *79*, 926.

(16) Mahoney, M. W.; Jorgensen, W. L. *J. Chem. Phys.* **2000**, *112*, 8910.

(17) Price, D. J.; Brooks, C. L., III *J. Chem. Phys.* **2004**, *121*, 10096.

(18) Horn, H. W.; Swope, W. C.; Pitera, J. W.; Madura, J. D.; Dick, T. J.; Hura, G. L.; Head-Gordon, T. *J. Chem. Phys.* **2004**, *120*, 9665.

(19) Rick, S. W. *J. Chem. Phys.* **2004**, *120*, 6085.

(20) Reimers, J. R.; Watts, R. O. *Mol. Phys.* **1984**, *52*, 357. In eq 24c, replace $2R_o$ by R_o. Burnham, C. J.; Xantheas, S. S. *J. Chem. Phys.* **2002**, *116*, 5115.

(21) Chen, B.; Xing, J.; Siepmann, J. I. *J. Phys. Chem. B* **2000**, *104*, 2391.

(22) Becke, A. *Phys. Rev. A* **1988**, *38*, 3098. Lee, C.; Yang, W.; Parr, R. G. *Phys. Rev. B* **1988**, *37*, 785.

(23) Troullier, N.; Martins, J. L. *Phys. Rev. B* **1991**, *43*, 1993.

(24) Tuckerman, M. E.; Yarne, D. A.; Samuelson, S. O.; Hughes, A. L.; Martyna, G. J. *Comput. Phys. Commun.* **2000**, *128*, 333.

(25) Tassone, F.; Mauri, F.; Car, R. *Phys. Rev. B* **1994**, *50*, 10561.

(26) Nosé, S. *Mol. Phys.* **1984**, *52*, 255. Hoover, W. G. *Phys. Rev. A* **1985**, *31*, 1695.

(27) Martyna, G. J.; Tuckerman, M. E.; Klein, M. L. *J. Chem. Phys.* **1992**, *97*, 2635.

(28) Hutter, J.; Tuckerman, M.; Parrinello, M. *J. Chem. Phys.* **1995**, *102*, 859.

(29) Chen, B.; Ivanov, I.; Park, J. M.; Parrinello, M.; Klein, M. L. *J. Phys. Chem. B* **2002**, *106*, 12006.

(30) Chen, B.; Ivanov, I.; Klein, M. L.; Parrinello, M. *Phys. Rev. Lett.* **2003**, *91*, 215503.

(31) Chen, B.; Potoff, J.; Siepmann, J. I. *J. Phys. Chem. B* **2000**, *104*, 2378.

(32) Chen, B.; Siepmann, J. I. *Theor. Chem. Acc.* **1999**, *103*, 87.

(33) Izvekov, S.; Voth, G. A. *J. Chem. Phys.* **2002**, *116*, 10372.

(34) Hura, G.; Russo, D.; Glaeser, R. M.; Head-Gordon, T.; Krack, M.; Parrinello, M. *Phys. Chem. Chem. Phys.* **2003**, *5*, 1981.

(35) VandeVondale, J.; Mohamed, F.; Krack, M.; Hutter, J.; Sprik, M.; Parrinello, M. *J. Chem. Phys.* **2005**, *122*, 014515.

(36) McGrath, M. J.; Siepmann, J. I.; Kuo, I.-F. W.; Mundy, C. J.; VandeVondele, J.; Sprik, M.; Hutter, J.; Mohamed, F.; Krack, M.; Parrinello, M. *Comput. Phys. Commun.* **2005**, *169*, 289.

Figure 16. $g_2(r_{HO}, \omega_{HO_DH_D\cdots O_A})$ surface and contour plots of TIP3P ice I_h at 150 K (top) and liquid water at 300 K (bottom). Only contour lines ranging above 1.05 are shown.
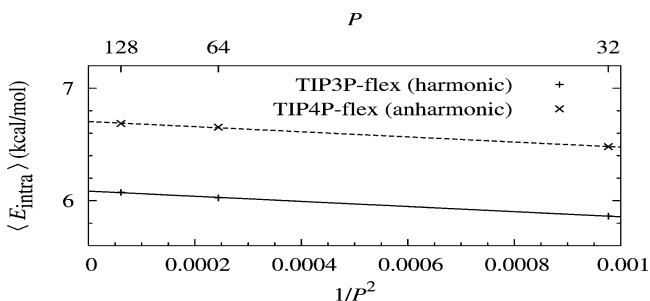

Figure 17. Intramolecular energy versus P of a TIP3P- or TIP4P-flex H_2O molecule. The best-fit lines are shown.

for a given δt. On the basis of all of these tests, the final parameters used to study TIP4P-flex-PI water are $\mathcal{T} = 200$ ps, $\delta t = 1.0$ fs, and $P = 64$ beads.

3554 *J. Phys. Chem. B, Vol. 110, No. 8, 2006*

Mantz et al.

(37) Kuo, I-F. W.; Mundy, C. J.; McGrath, M. J.; Siepmann, J. I.; VandeVondele, J.; Sprik, M.; Hutter, J.; Chen, B.; Klein, M. L.; Mohamed, F.; Krack, M.; Parrinello, M. *J. Phys. Chem. B* **2004**, *108*, 12990.

(38) Grossman, J. C.; Schwegler, E.; Draeger, E. W.; Gygi, F.; Galli, G. *J. Chem. Phys.* **2004**, *120*, 300.

(39) Allesch, M.; Schwegler, E.; Gygi, F.; Galli, G. *J. Chem. Phys.* **2004**, *120*, 5192.

(40) Schwegler, E.; Grossman, J. C.; Gygi, F.; Galli, G. *J. Chem. Phys.* **2004**, *121*, 5400.

(41) Kuo, I.-F. W.; Mundy, C. J. *Science* **2004**, *303*, 658.

(42) Silvestrelli, P. L.; Parrinello, M. *Phys. Rev. Lett.* **1999**, *82*, 3308.

(43) Silvestrelli, P. L.; Parrinello, M. *J. Chem. Phys.* **1999**, *111*, 3572.

(44) Shiga, M.; Tachikawa, M.; Miura, S. *J. Chem. Phys.* **2001**, *115*, 9149.

(45) Kuharski, R. A.; Rossky, P. J. *J. Chem. Phys.* **1985**, *82*, 5164.

(46) Stern, H. A.; Berne, B. J. *J. Chem. Phys.* **2001**, *115*, 7622.

(47) Svishchev, I. M.; Kusalik, P. G. *J. Chem. Phys.* **1993**, *99*, 3049. Kusalik, P. G.; Svishchev, I. M. *Science* **1994**, *265*, 1219. Svishchev, I. M.; Zassetsky, A. Y.; Kusalik, P. G. *Chem. Phys.* **2000**, *258*, 181

(48) Soper, A. K. *J. Chem. Phys.* **1994**, *101*, 6888.

(49) Luzar, A.; Chandler, D. *Phys. Rev. Lett.* **1996**, *76*, 928.

(50) Lazaridis, T.; Karplus, M. *J. Chem. Phys.* **1996**, *105*, 4294.

(51) Santis, A. D.; Rocca, D. *J. Chem. Phys.* **1997**, *107*, 9559.

(52) Kolafa, J.; Nezbeda, I. *Mol. Phys.* **2000**, *98*, 1505.

(53) Flükiger, P.; Lüthi, H. P.; Portmann, S.; Weber, J. *MOLEKEL*, version 4.0; Swiss Center for Scientific Computing: Manno Switzerland, 2000.

(54) Humphrey, W.; Dalke, A.; Schulten, K. *J. Mol. Graphics* **1996**, *14*, 33 (*VMD*, version 1.8.2).

(55) Brooks, B. R.; Bruccoleri, R. E.; Olafson, B. D.; States, D. J.; Swaminathan, S. *J. Comput. Chem.* **1983**, *4*, 187.

(56) Barker, J. A. *J. Chem. Phys.* **1979**, *70*, 2914.

(57) Herman, M. F.; Bruskin, E. J.; Berne, B. J. *J. Chem. Phys.* **1982**, *76*, 5150.